

Local-Resonance-Induced Dual-Band Topological Corner States of Flexural Waves in a Perforated Metaplate

Lei Fan,¹ Yafeng Chen^{1,2,*}, Shuowei An¹, Tuo Liu³, Haiyan Fan,¹ Jie Zhu^{4,†} and Zhongqing Su^{1,5,‡}


¹*Department of Mechanical Engineering, The Hong Kong Polytechnic University, Kowloon, Hong Kong SAR, China*

²*State Key Laboratory of Advanced Design and Manufacturing for Vehicle Body, Hunan University, Changsha, Hunan 410082, People's Republic of China*

³*Key Laboratory of Noise and Vibration Research, Institute of Acoustics, Chinese Academy of Sciences, Beijing 100190, People's Republic of China*

⁴*School of Physics Science and Engineering, Tongji University, Shanghai 200092, People's Republic of China*

⁵*The Hong Kong Polytechnic University Shenzhen Research Institute, Shenzhen 518057, People's Republic of China*

 (Received 12 November 2022; accepted 13 February 2023; published 21 March 2023)

Despite their proven effectiveness in localizing and steering subwavelength elastic waves, locally resonant elastic topological insulators (TIs) with surface-mounted or embedded resonators are often challenged because of their structural complexity and the difficulty in realizing multiple topological band gaps. Here we present a second-order elastic TI (SETI), made of a perforated metaplate with a series of etched C-shaped slots, to achieve dual-band topological corner states. The etched slots in the metaplate form a type of cantileverlike oscillator, the multimodal bending resonances of which couple with the flexural vibration modes of the metaplate, resulting in multiple locally resonant band gaps. Judiciously configuring these slots in a C_{4v} -symmetric lattice enables topologically distinct metastructures and creates a SETI. We numerically and experimentally observe the dual-band corner states in two broad topological band gaps. Our platform for observing the topological effects in a perforated metaplate greatly simplifies the fabrication of metastructures for implementing locally resonant elastic TIs, benefiting applications of TIs at the subwavelength scale such as elastic wave trapping and energy amplification.

DOI: [10.1103/PhysRevApplied.19.034065](https://doi.org/10.1103/PhysRevApplied.19.034065)

I. INTRODUCTION

A recent quantum leap in the theory of topology has entailed the use of innovative topological insulators (TIs) in manipulation of optical [1–3], acoustic [4–6], and elastic waves [7–10]. The motivation is that the topological edge states, which are tightly bound at the domain wall between two topologically distinct domains, are immune to energy loss and backscattering from defects, discontinuities, or corners in the media [11–13]. TIs have proven effectiveness in robustly and flexibly manipulating elastic waves to achieve some highly localized attributes, and thus endowing conventional functional materials for elastic wave manipulation with great potential, such as loss-free wave communication [14] and local wavefield magnification [15]. With continued efforts, the structural topologies of elastic TIs have progressed from discrete spring-mass

systems [16] to continuous mechanical structures [17–21] with a variety of topological effects, as typified by quantum Hall insulators [16], quantum spin Hall insulators [17–19], and valley Hall TIs [20], which have been realized in accordance with bulk-boundary correspondence, supporting gapless edge states.

However, the topological effects realized in these elastic systems are typically restricted at ultrasonic frequencies because most elastic TIs rely on Bragg scattering to create a topological band gap (i.e., the gap hosting a topological state), thus their operating frequencies are constrained by the lattice constants of the periodic medium. Recognition of this limitation has triggered the endeavor to explore the realization of subwavelength elastic TIs. To this end, it is a common practice to incorporate locally resonant elements, such as surface-mounted or embedded resonators [22–25], into an elastic topological structure. As a result, the operating frequency of an elastic TI can be regulated to be close to the resonant frequency of the resonators [26–28]. Despite the use of resonators in these designs, topological states still exist within the topological

*yfchen@hnu.edu.cn

†jiezhu@tongji.edu.cn

‡zhongqing.su@polyu.edu.hk

band gap opened by the Bragg scattering rather than by the local resonance [29–31]. Subsequently, locally resonant topological band gaps, which are formed by opening the local-resonance-created degenerate points, have been demonstrated to support topological edge states [29,32–35]. However, the introduction of local resonators is at the cost of complicating the metastructures and imposing difficulties in system modeling, given the imperfect contacts between the resonators and the host structure. In addition, topological band gaps created by the local resonance [29,32–35] typically possess narrow bandwidths, limiting the localization degree of topological waves.

In addition to the effort of reducing the operating frequency of TIs, attempts to create multiband topological effects have been increasing [36–39]. Multiband topological effects have enriched the topological family and enabled several applications such as multiband amplification of acoustic waves [40]. Compared with TIs with a single topological band gap, the TIs realizing multiband topological effects are typically characterized by a higher degree of geometrical complexity, necessitating alternative design strategies such as inverse design methods [41,42]. In particular, for an elastic structure capable of generating multiple band gaps, irrespective of the mechanisms adopted, the multiband topological states are anticipated to be achieved by simultaneously triggering the topological effects within the dual or multiple band gaps. Representative examples include the dual-band topological interface states within the Bragg and locally resonant topological band gaps of a one-dimensional structure [36], and dual-band topological states using mixed Lamb wave modes [39].

Another sort of advanced TI with hierarchically topological properties has recently been reported, known as second-order TIs (SOTIs), and these have been demonstrated to be effective in hosting zero-dimensional corner states [43–50]. In a similar vein, different types of second-order elastic TIs (SETIs) have been implemented [51–58]. The underlying physics of SETIs substantially relies on the crystalline symmetry of the periodic elastic media [51–58], and SETIs are commonly created by shrinking, expanding, or rotating scatters in the unit cells with various symmetries, including the hexagonal lattice with C_{6v} [51,52] and C_3 [53,54] symmetries, the kagome lattice with C_{3v} symmetry [55], and the square lattice with C_4 symmetry [56–58].

Owing to their structural complexity, local-resonance-induced SETIs, not to mention local-resonance-stimulated dual-band or multiband SETIs, have rarely been reported up to now. Despite recent advances in the theory of SETIs, there is still a need to realize dual-band topological corner states induced by local resonance in generic elastic structures. Motivated by this, we provide a simple and effective metaplate platform to realize a dual-band SETI: a series of C-shaped slots are etched into the elastic plate

to form several cantileverlike oscillating discs, the multimodal bending resonances of which open more than one locally resonant band gap, without relying on mounting resonators on the plate surface. These multiple band gaps, along with the inherent C_{4v} symmetry, provide the possibility of multiband topological corner states. Notably, the resonance-induced topological effect is herein realized using a single-phase perforated metaplate with a streamlined fabrication process compared with that of conventional metastructures with surface-mounted or embedded local resonators. This study explores the topological effects triggered by the local resonance in a C_{4v} -symmetric elastic structure [57,58], instead of the C_3 -symmetric and C_6 -symmetric structures under intensive investigation. In addition to dual-band corner states associated with bending resonances, at the end of the article, we also reveal the existence of the third topological state for flexural waves, which is induced by torsional resonance. Utilizing a perforated metaplate for realization of dual-band corner states extends the applicability of subwavelength SETIs.

II. RESULTS AND DISCUSSION

A. Modeling and analysis

Consider an elastic metaplate composed of a 2-mm-thick aluminum plate etched with a lattice of C_{4v} -symmetric C-shaped slots, unit cells of which are boxed in Fig. 1(a). These slots are similar to split-ring resonators in acoustic systems [30,31,59], in which they serve as Helmholtz cavities for manipulating subwavelength acoustic waves. In this research, the specific perforation engraves out cantileverlike oscillating discs, multimodal bending resonances of which couple with out-of-plane vibrations of the host plate and contribute to opening multiple flexural band gaps. Compared with previous locally resonant elastic TIs that employ surface-mounted resonators like pillars [12,13], the designed perforated metaplate allows for much simpler implementation while maintaining more accurate modeling because there is no coupling layer between the attached resonators and the host structure.

First, the dispersion characteristics (band diagrams) of the designed unit cells are calculated. Previous investigations on SOTIs with C_{4v} -symmetric lattices revealed that topologically distinct structures can be created by selecting different unit cells from the same periodic structure, the underlying physics of which lies in the changes of inter- and intracell coupling strengths [42–44]. Thus, we here consider two units: one (U_1) is the unit cell with four slots with inward notches, as boxed by the red dotted line in Fig. 1(a), whereas the other (U_2) is the unit cell with four slots with outward notches (boxed by the green dotted lines). Clearly, U_1 can turn into U_2 by translating the selection box through the distance ($a/2$, $a/2$) (lattice

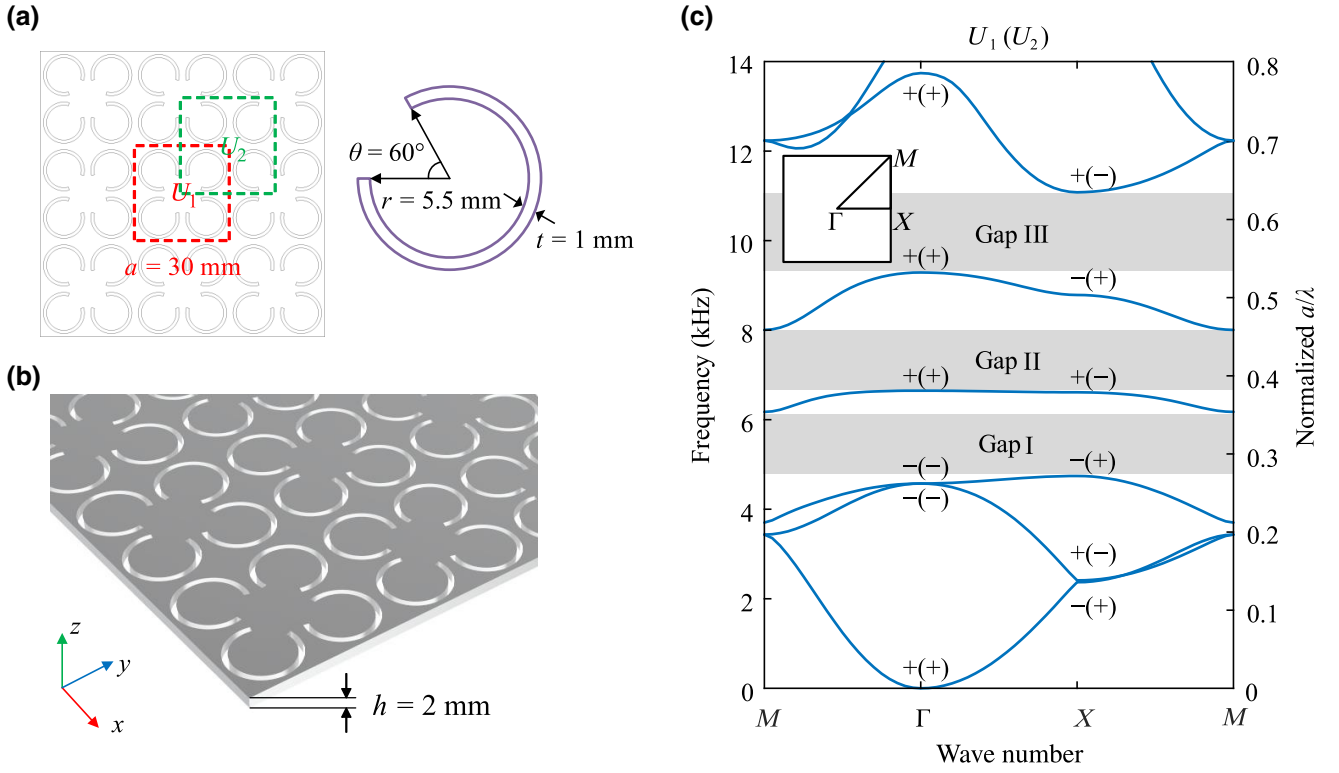


FIG. 1. (a) Unit cells U_1 and U_2 by different selection manners (top view), and slots' geometrical parameters including inner radius r , notch angle θ , and width of slots t . (b) The 3D schematic diagram of the perforated plate with thickness $h = 2$ mm. (c) Band diagram of U_1 (U_2) with marked parities at Γ and X where only bands representing out-of-plane displacements (along z axis) are shown.

constant $a = 30$ mm). From the standpoint of infinite periodicity, U_1 and U_2 should have identical dispersion curves (band diagrams) because they constitute the same periodical structure. Figure 1(c) illustrates the calculated band diagram of the unit cell U_1 (U_2), within which only the out-of-plane polarization modes are shown. To emphasize the subwavelength characteristic of locally resonant band gaps, the normalized frequency $\Omega = a/\lambda$ is also presented (λ is the wavelength of flexural waves in a thin plate) [60],

$$\frac{1}{\lambda} = \frac{1}{2\pi} \frac{1}{\sqrt{h}} \sqrt[4]{\frac{E}{12\rho(1-\nu^2)\omega^2}}, \quad (1)$$

where parameters E , ρ , ν , ω , and h are Young's modulus, density, Poisson's ratio, angular frequency, and thickness of plate, respectively (with respective values given in Appendix A). From the dispersion diagram in Fig. 1(c), it can be seen that three band gaps (marked as I, II, III) exist below the bar when $\Omega = 0.8$, and they are located between the third and fourth bands, the fourth and fifth bands, and the fifth and sixth bands, respectively. The associated band-gap ranges are 4.745–6.175, 6.65–8.005, and 9.29–11.08 kHz, respectively. The discussions on how these three band gaps are relevant to multimodal bending resonances of etched oscillators are presented in

Appendix B. Although U_1 and U_2 have identical band diagrams, they may have distinct topological properties, as their inter- and intracell coupling strengths are different [42–44], which is examined in the following.

According to existing investigations on topological structures with C_{4v} symmetry [42–44,46], it is straightforward to use two-dimensional (2D) polarization $P = (P_x, P_y)$, for characterizing the topological properties of U_1 and U_2 for corresponding band gaps, and 2D polarization P is expressed as

$$P_i = \frac{1}{2} \left(\sum_n q_i^n \bmod 2 \right), (-1)^{q_i^n} = \frac{\eta_n(X_i)}{\eta_n(\Gamma)}, \quad (2)$$

where subscript i denotes the x or y direction in the 2D plane, $\sum_n q_i^n$ is the sum of q_i^n of all n bands below the gap, mod denotes the modulo operation, and η_n is the parity at the high-symmetry points Γ or X of the n th band. Here, we simplify the determination of topological properties of the C_{4v} -symmetric structure using the parities at high-symmetry points, rather than calculating the Berry connection using the Wilson loop method [61]. Specifically, in this study, the parities (\pm) at points Γ and X are derived by the symmetry of the out-of-plane displacement (z -axis) profiles of the eigenmodes: both monopolar and quadrupolar modes have positive parity (+), while

the dipolar mode has negative parity ($-$) [42,44]. Detailed displacement profiles at points Γ and X are given in Appendix C. Moreover, C_{4v} point-group symmetry implies that $P_x = P_y$. According to the parities ($+$ or $-$) marked at points Γ or X of bands 1–5 in Fig. 1(c), the 2D polarizations of U_1 are determined as $P = (0, 0)$ within gaps I and II, while $P = (1/2, 1/2)$ within gap III, but those of U_2 are $P = (1/2, 1/2)$ within gap I, while $P = (0, 0)$ within gaps II and III. In other words, U_1 and U_2 are topologically distinct within gaps I and III, but identical within gap II. With this in mind, we focus on gaps I and III and investigate potential topological states within them. According to the bulk-boundary correspondence [1–4], it can be inferred that the topological edge states are expected to appear within gaps I and III at the domain wall between two topologically different regions composed of U_1 and U_2 , respectively. Furthermore, the topological corner charge index, defined by $Q^c = 4P_x P_y$ [42,45,46], indicates that U_1 and U_2 have different corner charge values (one is zero while the other is not) within gaps I and III, implying the existence of corner states at the corners of domain walls. In addition, it can be noted that the two topological band gaps (gap I and gap III), associated with the bending resonances of the engraved oscillators, possess a wider relative bandwidth compared with those of classical locally resonant topological metamaterials [29,32–34], which have complicated resonant elements and additional weight, providing room for producing more localized topological states.

To visualize topological edge states, we create a ribbon-shaped supercell [Fig. 2(a)] consisting of six U_1 units and six U_2 units, between which an interface (domain wall) for cultivating edge states is formed. Figure 2(b) shows the calculated dispersion of the supercell, from which one can see that the two topological edge states (highlighted with green dots) are formed within gaps I and III. The displacement profiles of these two edge states at $k_x = 0.5\pi/a$ further reveal their topological edge state characteristic, corresponding to highly localized energy at the domain wall, as illustrated in Fig. 2(c). It should also be noted that these two edge states are gapped within corresponding topological bulk band gaps, leaving a space for the advent of higher-order corner states [42–58]. Some boundary modes can also be discovered within the three band gaps in addition to the topological edge states at the domain wall. The presence of high energy localization at the upper and lower boundaries of the ribbon rather than the domain wall in the displacement profiles of these boundary modes, as seen in Fig. 2(d), arises from the simulation’s use of free boundary conditions. It is noteworthy that edge states are also likely to appear at external boundaries of a single topologically nontrivial structure when boundary conditions are free [51]. Discussing the origin of these boundary modes is outside the scope of the current work because we focus only on topological states appearing at the domain wall in this study. The conclusion drawn from earlier polarization analysis—that band gap II is incapable of hosting

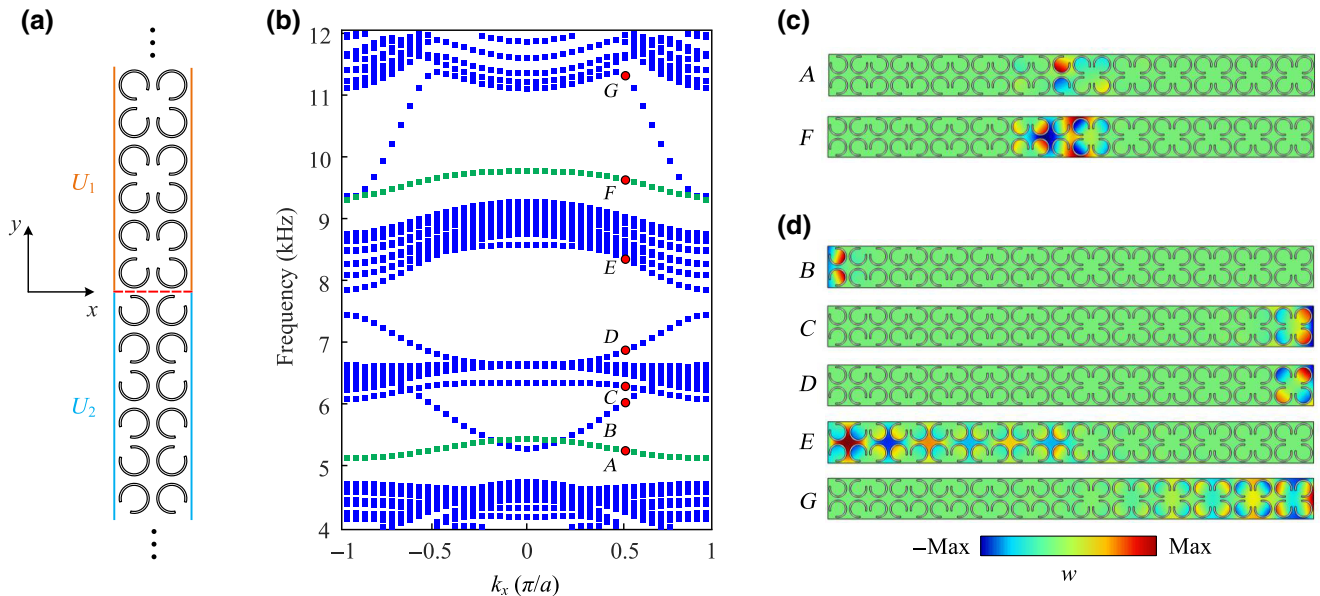


FIG. 2. (a) Schematic diagram of ribbon-shaped supercell, in which red dotted line represents domain wall. In numerical simulation for calculating supercell dispersion, left and right edges are applied with Floquet-Bloch boundary conditions, while upper and lower ends are stress-free. (b) Dispersion of the supercell where topological edge states appearing at the domain wall are labeled with green dots, and other branches at band-gap frequencies represent boundary modes. (c),(d) Out-of-plane displacement profiles (z -axis displacement w) at red dots labeled in (b) for (c) topological edge states and (d) boundary modes.

topological edge states at the domain wall—is supported by the fact that gap II only contains boundary modes and lacks any localized states at the domain wall. Additionally, it is inferred from mechanical displacement fields in Figs. 2(c) and 2(d) that bending modes of these etched resonators play a crucial role in the formation of these multiple band gaps. Detailed discussion can be seen in Appendix B.

To prove the existence of topological corner states within gaps I and III, we construct a finite-size square plate consisting of 5×5 U_1 cells surrounded by three layers of U_2 cells, and then perform the eigenfrequency analysis. The box-shaped sample allows us to observe topological edge states at domain walls and corner states at 90° bends of domain walls. In the numerical simulation, the boundary conditions of the entire metaplate are set to be

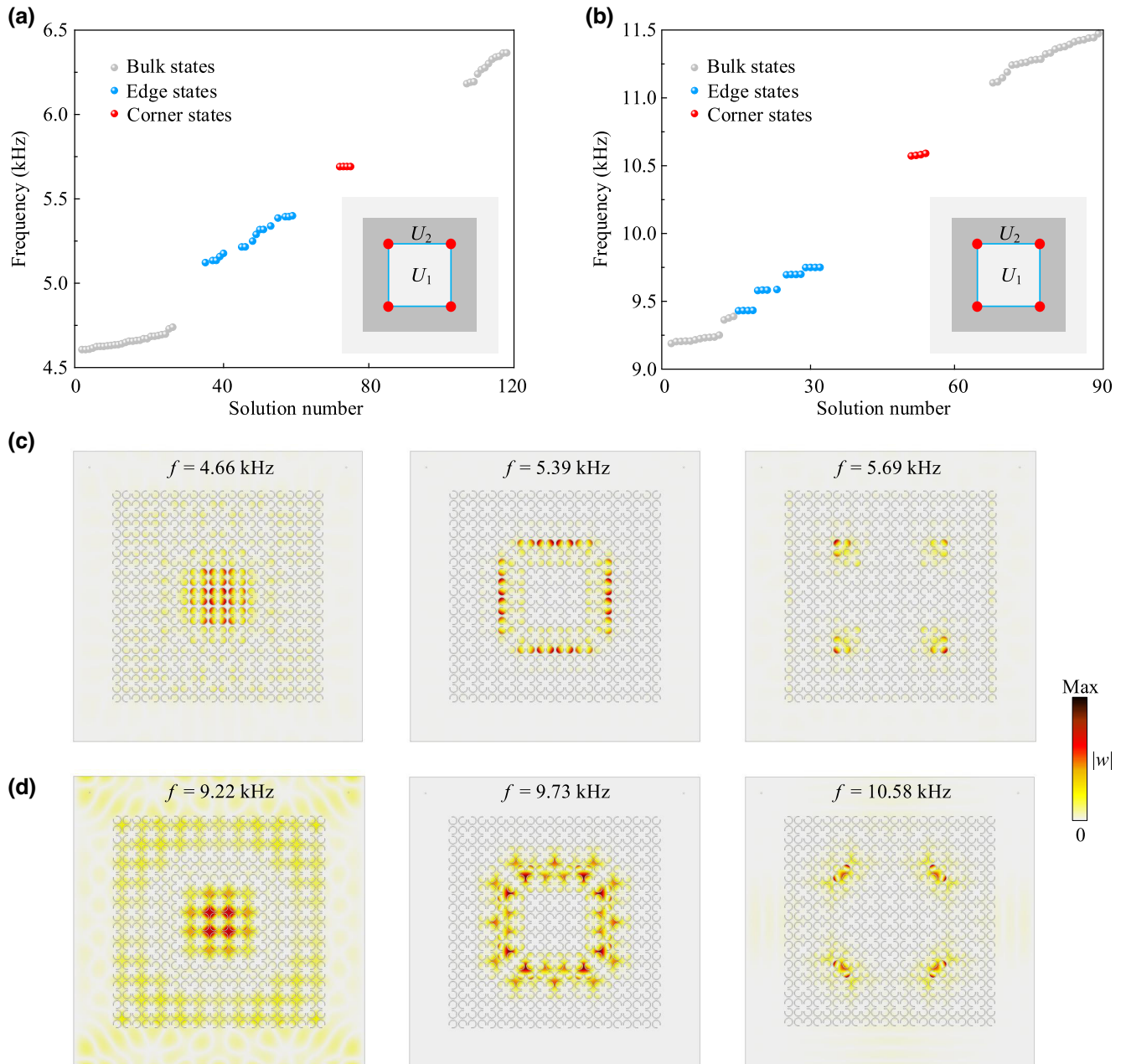


FIG. 3. (a),(b) Eigenfrequencies of square plate calculated around frequency domains of (a) gap I and (b) gap III, in which only bulk, edge, and corner states are displayed while other irrelevant modes are hidden. (c),(d) Absolute out-of-plane displacement profiles (z -axis displacement w) at several selected frequencies in (a),(b), in which bulk, edge, and corner states are presented from left to right, respectively.

fixed for left and right edges and free for upper and lower edges, to be consistent with those of the subsequent experimental validation. The eigenfrequencies calculated around the frequency domains of gap I and gap III are shown in Figs. 3(a) and 3(b), in which eigenfrequencies of the bulk, edge, and corners states are displayed, whereas other irrelevant modes like boundary-condition-induced ones are hidden. Within both gaps, a cluster of topological edge states (blue dots) appear from 5.12 to 5.4 kHz for gap I and from 9.45 to 9.75 kHz for gap III, featuring the high energy localization at domain walls, referring to the selected fields at 5.39 and 9.73 kHz in Figs. 3(c) and 3(d). Figures 3(a) and 3(b) show that four nearly degenerate corner states (red dots) appear at around 5.7 kHz for gap I and at around 10.6 kHz for gap III within associated edge gaps, which feature high energy localization at the corners

of nearby domain walls, referring to the selected displacement profiles at 5.69 and 10.58 kHz in Figs. 3(c) and 3(d). In contrast, flexural waves spread over the entire plate for bulk states, as seen in fields at 4.66 and 9.22 kHz.

B. Experimental validation

Experimental demonstration is accomplished using a laser Doppler vibrometer to validate the numerically calculated dual-band corner states. A 6061-aluminum alloy plate ($450 \times 450 \text{ mm}^2$) fabricated by laser-cutting technology is prepared, with its size and boundary conditions being identical to those in the simulation described previously. The detailed experimental setup and implementation are given Appendix F. Given that the sample contains four corners, we measure 4 times in total in order to observe

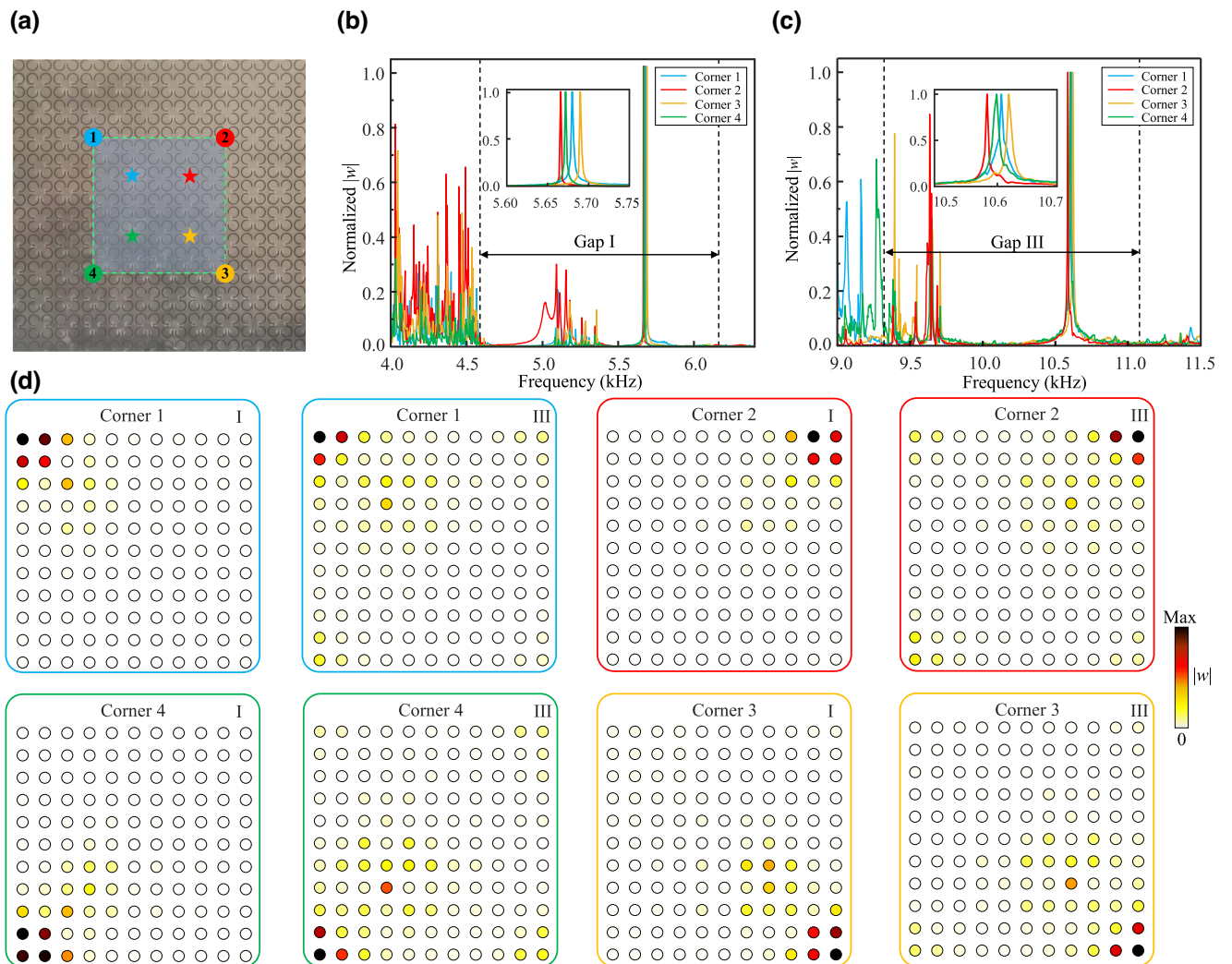


FIG. 4. (a) Excitation and detection locations in the sample for each measurement in the experiment. The four measurements are distinguished by different colors (ordered by number); the stars denote excitation sources and circles are detection points. The response spectra of four corners within (b) gap I and (c) gap III. The insets in (b),(c) enlarge the response peaks corresponding to four corner states. (d) Experimentally measured displacement profiles at peak frequencies in (b),(c) corresponding to four pairs of dual-band corner states, where the notation at the top right represents gaps I and III.

four corner states separately. For each measurement, the transmission responses of a series of discrete points inside the domain wall [i.e., the region surrounded by the green dotted lines in Fig. 4(a)] are extracted to build displacement fields later. Detailed scan points in the experiment can be seen in Appendix F. To detect dual-band corner states separately, the experimental frequency sweeping ranges are divided into two subsections: 4.0–6.4 kHz covering gap I and 9.0–11.5 kHz covering gap III.

In each measurement (distinguished by different colors), a pointlike excitation source is placed at around a quarter diagonal (labeled by stars) of the scan region and the detection point is placed at the corresponding corner (ordered by number), as seen in Fig. 4(a). Despite the fact that the excitation source is not placed exactly at the corner, the corner state is still expected to be excited effectively [57]. Figures 4(b) and 4(c) present the response-to-excitation spectra at the four corners within the two targeted frequency ranges, amplitudes of which are normalized by corresponding maximum value. As depicted by the response curves, for each corner, an obvious resonance peak is observed at about 5.7 kHz for gap I and at circa 10.6 kHz for gap III, frequencies of which are in good agreement with the results of corner state frequencies in the eigenfrequency simulation [Figs. 3(a) and 3(b)]. Insets in the response spectra of Figs. 4(b) and 4(c) show minor frequency differences among these peaks, which can be attributable to several inevitable factors in experiments, such as slight structural difference between the four corners in the manufactured sample, noise signals at each measurement, and imperfect boundary conditions caused by fixtures. The laser-scanned displacement fields of out-of-plane vibrations at these peak frequencies are displayed in Fig. 4(d), where the localized energy is highly confined around the corresponding corners, providing the evidence that these response peaks exactly represent topological corner states. Edge and bulk states could be also stimulated by the same excitation sources and corresponding experimental results are given in Appendix G. Additionally, influences of geometrical parameters (including the scalability) on these corner states and their robustness are numerically investigated, as presented in Appendices D and E, respectively. Besides the aforementioned dual-band topological corner states, which relate to the bending resonance of the engraved resonators, we highlight that the proposed metaplate also enables an unusual type of corner state for flexural waves that arises from torsional resonance at higher frequencies (gap IV), and corresponding numerical results are presented in Appendix H.

III. CONCLUSIONS

In this study, we design a perforated metaplate for realizing a local resonance-induced SETI, and on this platform, we successfully observe dual-band topological

corner states. This microperforated metaplate with elaborately etched C-shaped slots creates a series of cantilever-like oscillators, multimodal bending resonances of which couple with flexural vibration modes of the host plate, enabling dual topological band gaps. The topologically distinct structures characterized by 2D polarizations are constructed by selecting different unit cells, U_1 and U_2 , in the metaplate with C_{4v} -symmetric slots. As a result, we demonstrate numerically and experimentally that dual-band topological corner states emerge when topologically distinct structures built of U_1 and U_2 are connected, as evidenced by the high energy localization at the corners of the domain wall. Compared with prevailing locally resonant elastic TIs, this simple metaplate, which requires only easily achievable penetration, exhibits several advantages, such as high-accuracy fabrication, low-cost implementation, and excellent scalability, thus facilitating the use of topological devices in practice. The developed SETI with highly localized dual-band corner states can benefit applications of TIs such as subwavelength elastic wave trapping and energy harvesting [62].

ACKNOWLEDGMENTS

This work is supported by the Fundamental Research Funds for the Central Universities (Grant No. 22120220237), the Research Grants Council of Hong Kong SAR (Grants No. AoE/P-502/20, No. 15200922, No. 15202820, and No. 15205219), the Hong Kong Scholars Program (Grant No. XJ2020004), the National Natural Science Foundation of China (Grant No. 1210020421), and the Natural Science Foundation of Hunan Province (Grant No. 2022JJ40026). Z.S. acknowledges the support from Hong Kong Innovation and Technology Commission via project “Smart Railway Technology and Applications” (Grant No. K-BBY1)

APPENDIX A: NUMERICAL SIMULATION METHOD

Numerical simulations involving the calculation of unit-cell band diagrams, supercell dispersion, and eigenfrequency analysis are all performed by commercial finite element software COMSOL Multiphysics 5.6 using the 2D Plate module. The aluminum is modeled with Young’s modulus $E = 70 (1 + 0.008i)$ GPa, Poisson’s ratio $\nu = 0.33$, and density $\rho = 2700$ kg/m³, where the imaginary part of the modulus approximates the damping of the experimental sample. The 2D Plate module in COMSOL is based on Mindlin plate theory [63], which can accurately model the thin-plate structure. The resulting band diagram is compared with those of the three-dimensional (3D) Solid Mechanics module of COMSOL to validate the high accuracy of the 2D Plate module, as depicted in Fig. 5.

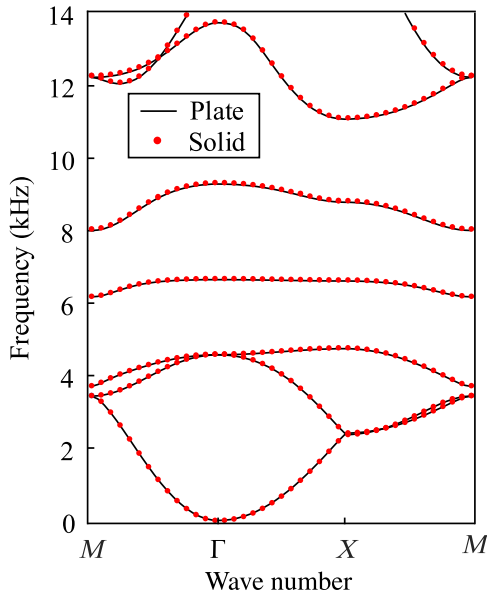


FIG. 5. Comparison of numerical results of band diagrams calculated by 2D Plate and 3D Solid Mechanics modules in COMSOL, in which only bands that represent out-of-plane (z -axis) displacement modes are plotted.

APPENDIX B: DISCUSSION ON ORIGIN AND PROPERTIES OF MULTIPLE BAND GAPS

We discuss how bending resonances of etched oscillators are related to three existing band gaps—gaps I, II, and III. The unit cell consisting of four slots with the same notch orientation angles can be regarded as the composite unit cell by doubling the lattice along the x and y directions of its $1/4$ part (primitive unit), as shown in Fig. 6(a). Figure 7(a) depicts the band dispersion of the primitive unit cell, in which a typical locally resonant complete band gap

is identified by Bloch modal shapes at band-gap bounds [64]: at the lower gap bound, mechanical energy is strongly confined at the bending resonance of etched resonators, but the host plate (remaining parts of the unit cell) is nearly motionless, while the modal shape at the upper gap bound is characterized by coupling between the bending resonance of the etched resonator and the flexural vibration modes of the host plate. We call this complete band gap a primitive locally resonant band gap. When the primitive unit is expanded into the composite one, the Brillouin zone is shrunk [Fig. 6(b)] and band folding appears by the following principle [51]:

$$\begin{aligned}
 (M_2\Gamma_2)_{\text{composite}} &= (M_1M_2)_{\text{primitive}} + (X_1M_2)_{\text{primitive}} \\
 &\quad + (Y_1M_2)_{\text{primitive}} + (\Gamma_1M_2)_{\text{primitive}}, \\
 (\Gamma_2X_2)_{\text{composite}} &= (X_1X_2)_{\text{primitive}} + (Z_1M_1)_{\text{primitive}} \\
 &\quad + (Y_1Z_1)_{\text{primitive}} + (\Gamma_1X_2)_{\text{primitive}}, \\
 (X_2M_2)_{\text{composite}} &= (X_2M_2)_{\text{primitive}} + (X_2M_2)_{\text{primitive}} \\
 &\quad + (M_2Z_2)_{\text{primitive}} + (M_2Z_2)_{\text{primitive}}.
 \end{aligned} \tag{B1}$$

The corresponding band diagram of the composite unit is plotted in Fig. 7(b). The four slots in the composite unit initially maintain translational symmetry, and some bands overlap along the boundary line of the first Brillouin zone (X - M direction) for the third and fourth bands, as well as the fifth and sixth bands, as shown in Fig. 7(b). When slots are rotated to C_{4v} symmetry, the third and fourth bands, as well as the fifth and sixth bands are completely separated and eventually yield dual topological band gaps I and III, as shown in Fig. 7(c). On the other hand, each C_{4v} -symmetric unit cell that has four slots can be regarded as a

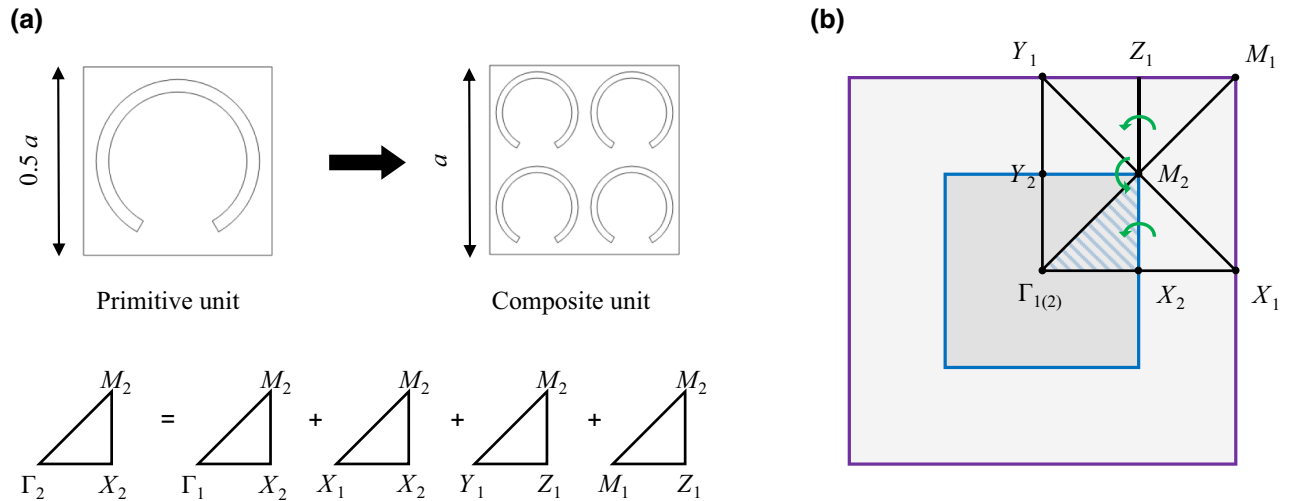


FIG. 6. (a) Primitive unit cell expanded into composite unit cell, and mapping relation of band-folding mechanism. (b) First Brillouin zones and high-symmetry points of primitive cell (boxed by purple line) and composite cell (boxed by blue line).

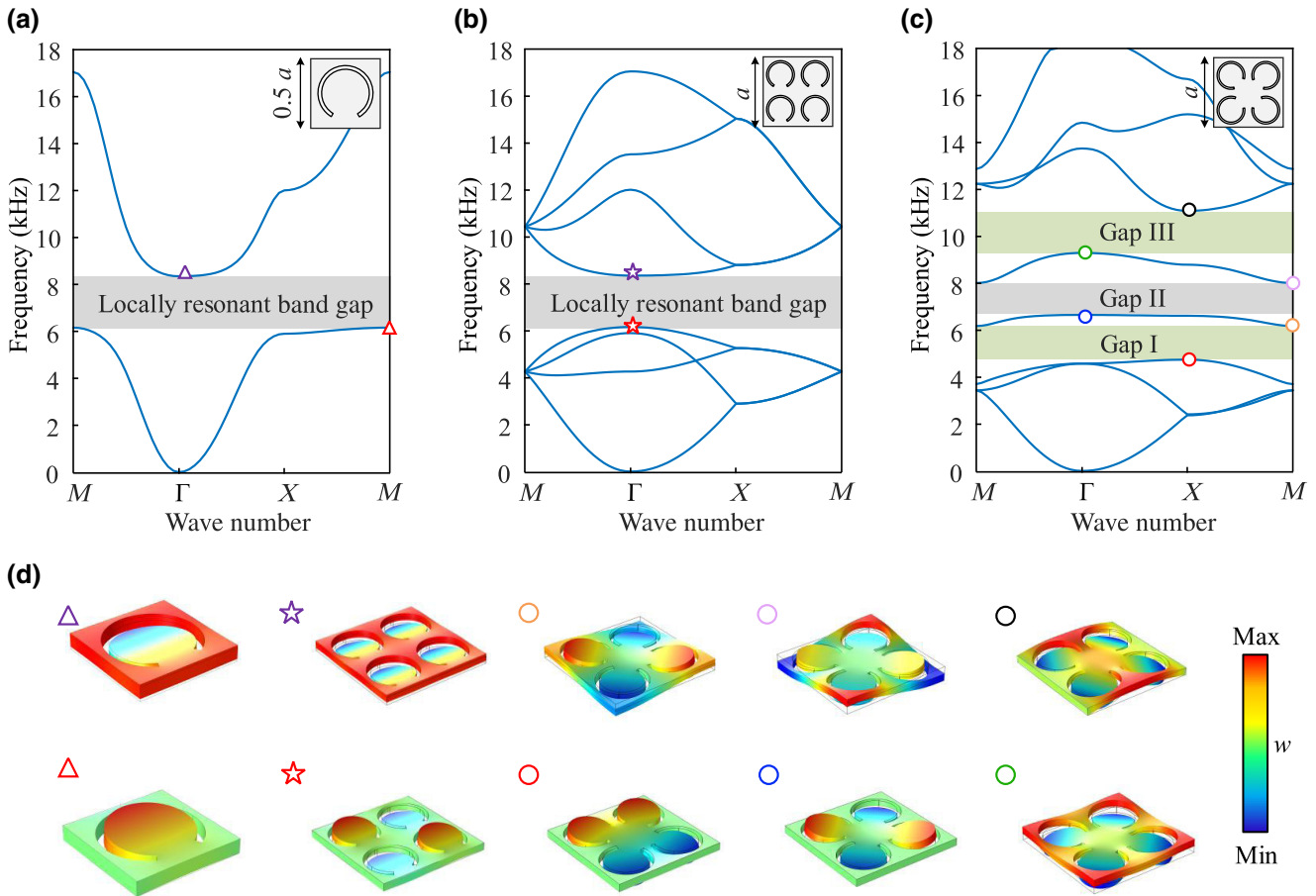


FIG. 7. Band diagrams of (a) primitive unit cell and (b) composite unit cell with four translationally symmetric slots, and (c) unit cell with C_{4v} -symmetric slots. (d) Modal shapes at points labeled in (a)–(c).

multiresonator system, and its multimodal bending vibrations contribute to these band gaps. Typically, at the lower bounds of each gap, four resonators bend in the dipolar mode for gap I, in the quadripolar mode for gap II, and in the monopolar mode for gap III, as indicated in Fig. 7(d). Conclusively, the multimodal bending modes of the four local resonators induce multiple flexural band gaps, while the inherent C_{4v} symmetry determines their topological natures.

APPENDIX C: DISPLACEMENT PROFILES OF THE FIRST SIX BANDS AT Γ AND X

The out-of-plane (z -axis) displacement profiles of eigenmodes at high-symmetry points Γ and X for unit cells U_1 and U_2 are presented in Fig. 8. The polarizations of these fields allow us to deduce the parities labeled in Fig. 1(c), and then relevant parities at Γ and X of the first three bands determine the topological properties of U_1 (U_2) within gap I while the parities at Γ and X of the first five bands determine topological properties of U_1 (U_2) within gap III.

APPENDIX D: INFLUENCES OF GEOMETRICAL PARAMETERS ON BAND GAPS AND CORNER STATES AND SCALABILITY

We investigate the influences of geometrical parameters on the frequencies of these multiple band gaps and resultant corner states. Figure 9 depicts the evolution of the frequencies of interest with different parameters: inner radius r , notch angle θ , width t of slots (shrinking or expanding inner radius r while fixing outer radius), and plate thickness h . It should be pointed out that when independently investigating one single parameter, the others remain the same as those in the main text.

It can be seen that the geometrical parameters of the slots have a significant influence on the width of the dual topological band gaps, thereby affecting the existence and frequencies of corner states: As topological gaps become wider, corner states are inclined to shift to the band-gap central frequency, which might induce higher energy confinement at the corners [65]. With a narrower band gap, the corner states may be hidden in the bulk states (dotted line in Fig. 9) or disappear. That is, we can tailor the frequencies of dual-band corner states in a wide range by fine

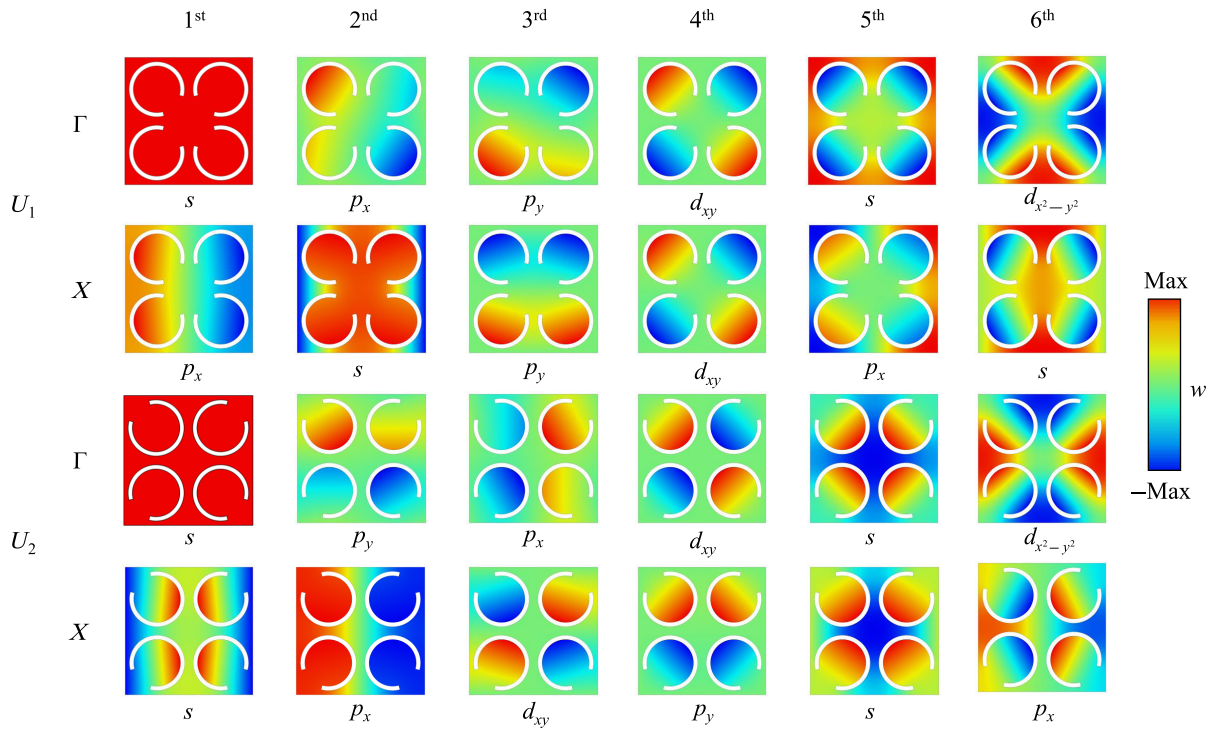


FIG. 8. The out-of-plane displacement (z -axis) profiles and their polarizations at Γ and X of the first six bands for U_1 and U_2 , where subscript s denotes monopolar, p_x and p_y represent dipolar, while d_{xy} and $d_{x^2-y^2}$ represent quadrupolar modes.

tuning the parameters of the slots with little modification to the structure.

Moreover, despite being demonstrated at low frequencies in this paper, our proposed perforation strategy

that enables topological states still works effectively in plate structures at ultrasound or even higher frequencies. Figure 9(d) shows that gaps I and III along with corresponding corner states shift to higher frequencies as plate

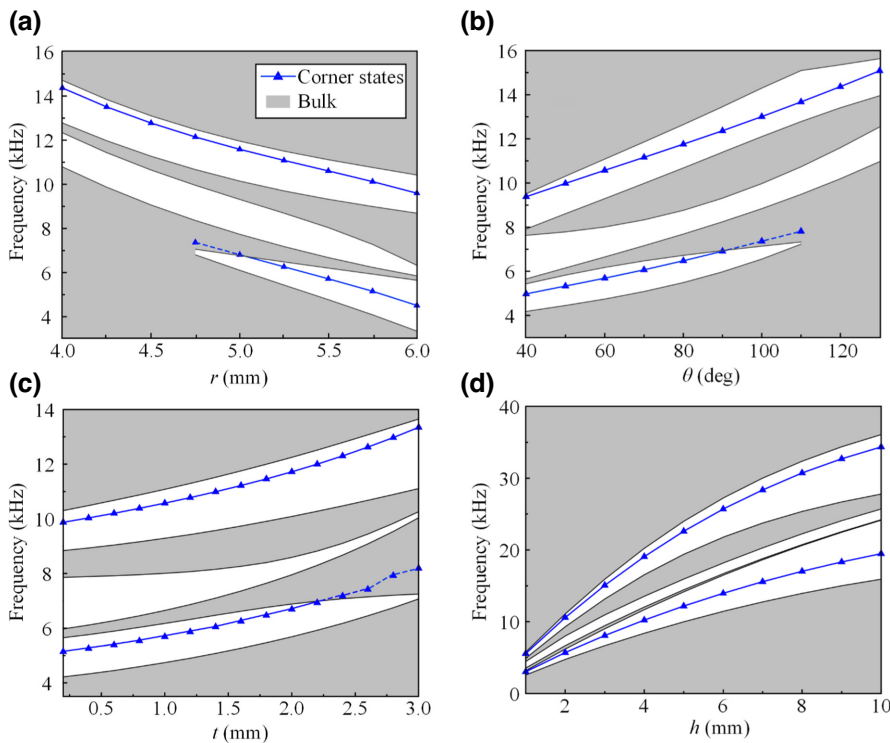


FIG. 9. Evolution of frequencies of band gaps and corner states with parameters (a) inner radius r , (b) notch angle θ , (c) width t of slots, and (d) plate thickness h . Dotted lines represent that corner states are hidden within the bulk.

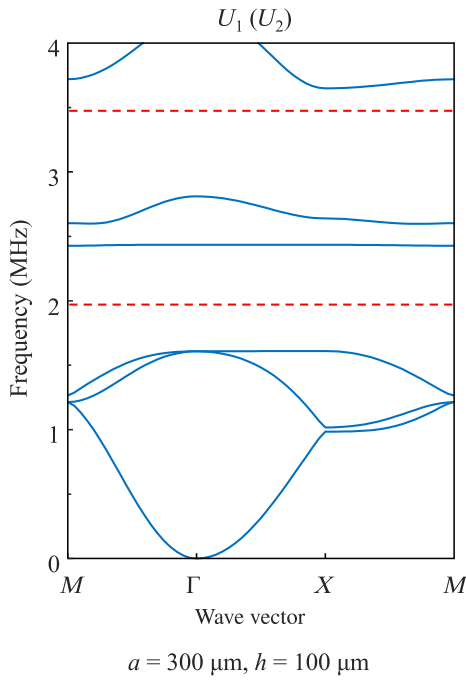


FIG. 10. Band structure of scaled down (100 times) unit cells U_1 and U_2 (thickness $h = 100 \mu\text{m}$), where two red dotted lines denote frequencies of dual-band corner states.

thickness h increases, and the relative bandwidths widen simultaneously.

Normally, reducing unit size also leads to higher working frequencies. Here, we consider an extreme case: the

unit size is scaled down 100 times, resulting in a lattice constant $a = 300 \mu\text{m}$. As illustrated in Fig. 10, now at megahertz frequencies, it can be seen that the microscale device (thickness $h = 100 \mu\text{m}$) has a similar dispersion and still holds dual-band topological corner states. The above parameter analysis reflects the good scalability of the proposed microperforated SETI, revealing that the underlying physics and mechanics are scale independent. So far, most existing on-chip elastic topological devices are commonly achieved by mounting scatterers on base materials like silicon wafers via photolithography techniques [57]. Solid structures with microperforations offer an alternative for on-chip elastic topological devices via several available techniques such as submicrometer-level laser cutting.

Conclusively, irrespective of the geometrical parameters and scale, these multiple topological band gaps always appear as long as well-shaped resonators remain intact, because topological band gaps are determined by inherent vibrational mechanisms and symmetry.

APPENDIX E: ROBUSTNESS OF CORNER STATES

We adopt a 1/4 model to examine the robustness of corner states. Eigenfrequencies are computed in an intact 1/4 metaplate and an imperfect 1/4 metaplate with a defect and a disorder (boxed by green solid lines in Fig. 11). Despite minor frequency deviations, the displacement profiles show that presence and high localization of dual

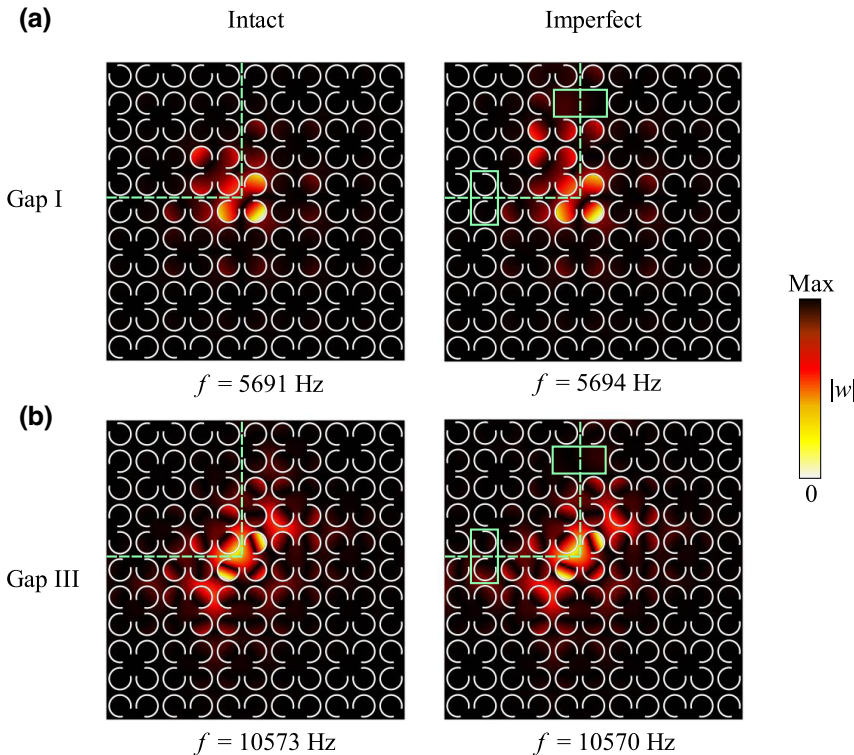


FIG. 11. Displacement fields at frequencies of corner states for an intact plate and an imperfect plate with disorder and defect within (a) gap I and (b) gap III. Green dotted line is domain wall and green solid boxes represent defect or disorder.

corner states within gaps I and III are immune to defect and disorder.

APPENDIX F: EXPERIMENTAL SETUP AND IMPLEMENTATION

The vibration in the out-of-plane direction is captured by the scanning laser vibrometer (PSV 400): the excitation signal (chirp) is amplified by a power amplifier (B&K 2706) and sent to the shaker in which a force transducer (B&K 8200) measures the resultant force at the excitation point. The recorded force signal is amplified through a charge amplifier (B&K 2635) and sent to a controller. In the meantime, the controller also receives displacement/velocity/acceleration signals directly measured from a laser vibrometer. The procedure diagram is illustrated in Fig. 12(a).

After Fourier transform, the frequency response function can be obtained,

$$H(\omega) = \frac{X(\omega)}{F(\omega)}, \quad (\text{F1})$$

where $F(\omega)$ is force input of the shaker and $X(\omega)$ is the displacement response at the detection points. In this article, values $|w|$ of response spectra in Figs. 4 and 13 refer to the $H(\omega)$ in Eq. (F1), which are then normalized by maximal value.

In the experiment, the sample is clamped at both left and right ends, as shown in Fig. 12(c). As a result, the left and right edges of the finite plate in the simulation have fixed constraint boundary conditions. For each measurement, 11×11 points in the area inside the domain wall are scanned in order to build the displacement profiles, as shown in Fig. 12(b).

APPENDIX G: EXPERIMENTAL RESULTS ON EDGE AND BULK STATES

Edge states and bulk states are illustrated using the results from the first measurement, where the excitation source is located close to the upper-left corner [labeled in Fig. 4(a)]. Figure 13(a) points out the detection locations for extracting the transmission spectra of edge, corner, and bulk states, distances of which towards the excitation point are identical. As seen in Figs. 13(b) and 13(c), owing to the

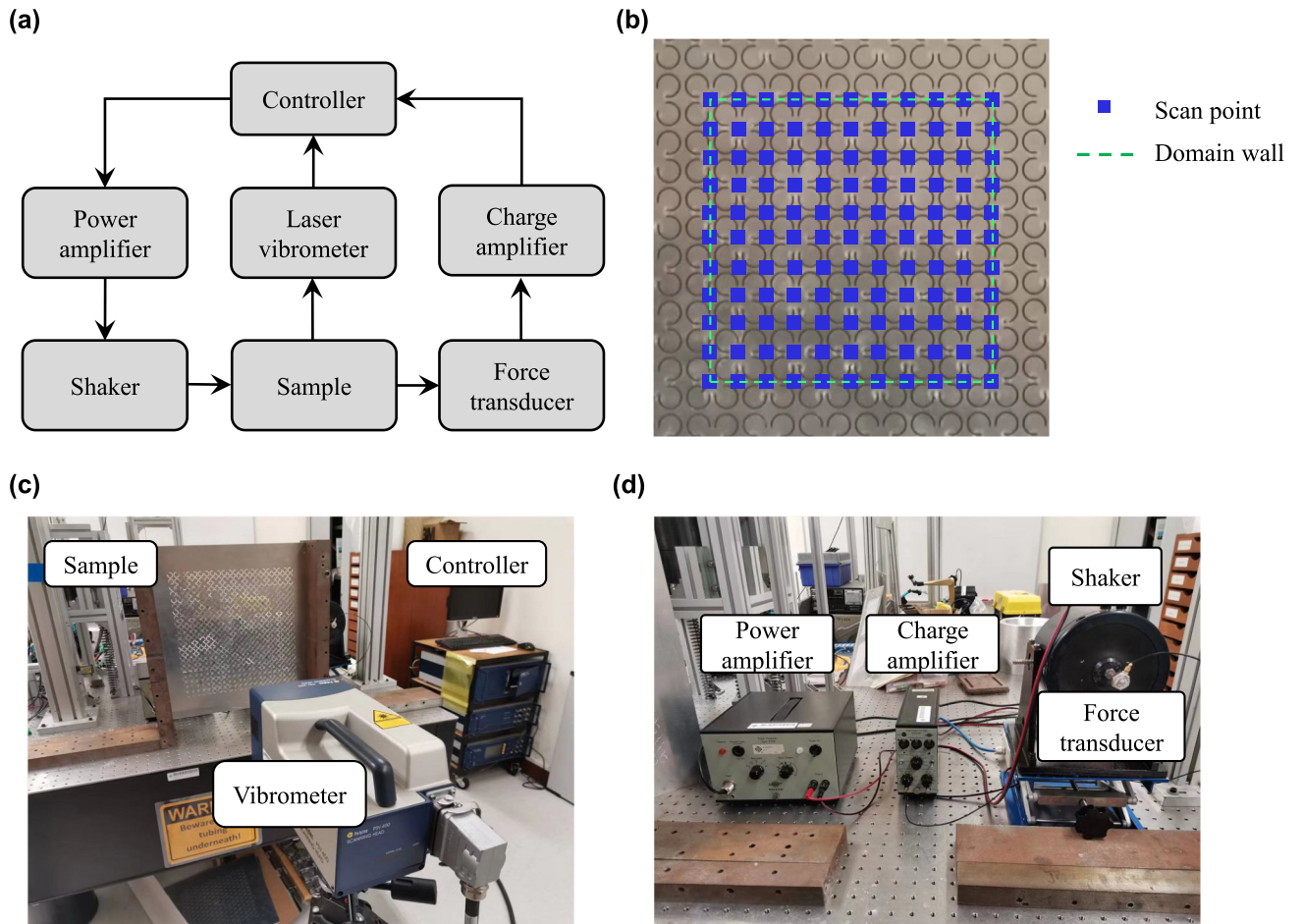


FIG. 12. (a) Procedures of measuring vibration responses of the sample. (b) Scanned region with 11×11 scan points. (c),(d) Photographs of experimental setups.

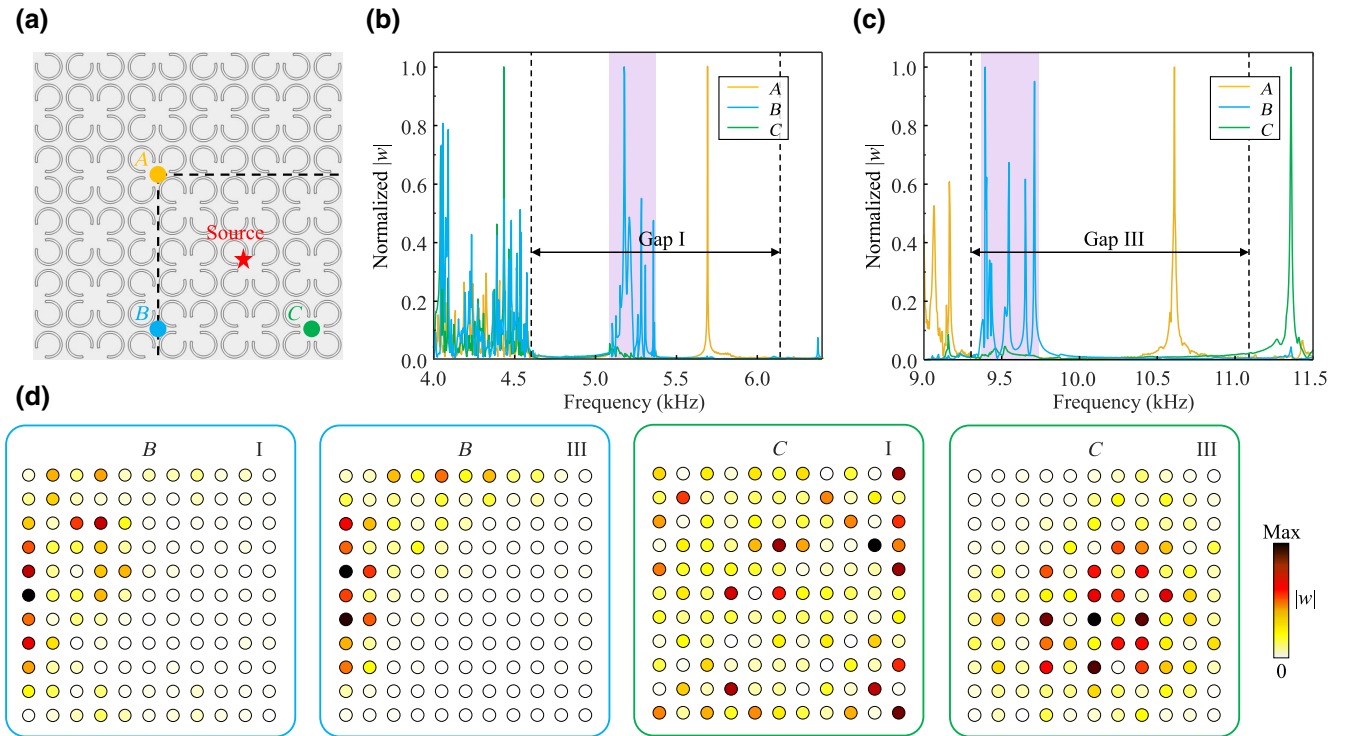


FIG. 13. (a) Excitation and detection positions for corner, edge, and bulk states, for which distances to excitation source are identical. (b),(c) Transmission spectra of detection points A , B , and C at frequency domains around (b) gap I and (c) gap III, in which purple shaded areas are the frequency domains of edge states. (d) Experimentally scanned displacement profiles at peak frequencies of responses at the point B and at the point C , corresponding to maximal values of green and blue curves in (b),(c).

band-gap effect, the transmission spectra of detection point C have very low energy in the domain of gaps I and III, whereas for detection point B , both gaps contain a cluster of high responses (shaded areas), which represent topological edge states, and their frequency ranges (from 5104 to 5380 Hz for gap I, and from 9378 to 9720 Hz for gap III) are in good agreement with those of the eigenfrequency results of Fig. 3. The displacement fields at response peaks of the B and C detection points indicate that topological edge waves localize at the left domain wall, while flexural waves at the bulk state frequencies spread over the plate, as shown in Fig. 13(d). It is noteworthy that Fig. 13(d) only depicts displacement fields at these selected peak frequencies for edge states; displacement responses at other edge state frequencies [shaded areas in Figs. 13(b) and 13(c)] exhibit diverse field profiles localizing at domain walls.

APPENDIX H: CORNER STATE INDUCED BY TORSIONAL RESONANCE

Besides dual-band topological corner states associated with the bending resonance of the engraved resonators, in the following, we demonstrate a particular type of

corner state for flexural waves, which is induced by torsional resonance. The topological band gap of interest is located between the ninth and tenth bands, referred as gap IV, as seen in Fig. 14(a). It is clear that gap IV arises from the torsional resonance of the engraved oscillators, evidenced by the eigenmode at the lower bound of the gap, see the inset of Fig. 14(a). According to the parities (listed in Table I) at high-symmetry points Γ and X of the first nine bands below the gap, U_1 is topologically nontrivial while U_2 is trivial within gap IV. As indicated in Fig. 14(b), the supercell dispersion (the same ribbon structure as in Fig. 2) shows that two branches of edge states (green dots) appear within gap IV, separated by an edge gap from 18 610 to 20 140 Hz. Next, a finite-sized plate comprised of $5 \times 5 U_1$ surrounded by five layers of U_2 is constructed and then its eigenfrequencies are calculated. As shown in Fig. 14(c), within gap IV, an eigenmode (the red dot) solely appears at 19 243 Hz, located between two branches of edge states (green dots). The field profile of this eigenmode [Fig. 14(d)], which features confined energy at the corner of domain walls, confirms that it certainly represents a corner state. Meanwhile, this topological corner state in gap IV is proved to be relevant to torsional resonance of engraved resonators,

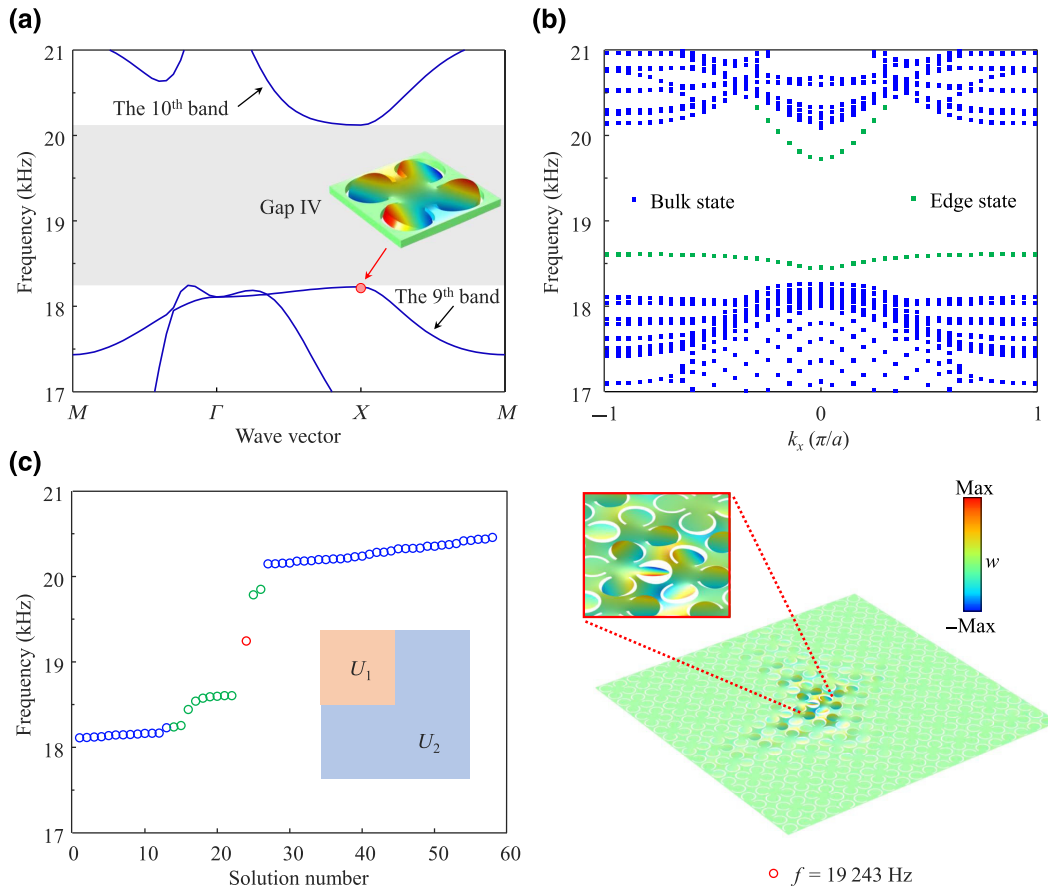


FIG. 14. Schematic diagrams of topological corner states induced by torsional resonance within gap IV. (a) Band structure for U_1 (the same as that of U_2) around gap IV, which is located between the ninth and tenth bands. Inset shows the mode shape at lower bound of gap IV (red dot), which implies the band gap is tied with torsional resonance of engraved resonators. (b) Supercell dispersion at frequencies around gap IV, and the sample for calculation is the same as the one in Fig. 2. Within the band-gap frequencies, only the pair of edge states (green dots) are plotted while other irrelevant boundary modes are hidden. (c) Eigenfrequencies of a finite-sized plate, where blue, green, and red dots represent bulk, edge, and corner states, respectively. Within the band-gap frequencies, other irrelevant eigenmodes like boundary modes are hidden. (d) Displacement field at the frequency of corner state [red dot in (c)] and its locally enlarged view, in which engraved resonators exhibit torsional resonances.

see the enlarged view in Fig. 14(d). That is, our design is able to trigger triband topological states, attributed to the rich vibration characteristics of engraved resonators. Furthermore, such torsional-resonance-induced topological states of flexural waves have never been reported, and may unlock unexplored physics for elastic TIs in the future.

TABLE I. Parities at high-symmetry points Γ and X of the first nine bands for U_1 and U_2 .

Unit cell	The order of band								
	1	2	3	4	5	6	7	8	9
U_1	Γ	+	-	-	+	+	+	-	-
	X	-	+	-	+	-	+	+	-
U_2	Γ	+	-	-	+	+	+	-	-
	X	+	-	+	-	+	-	+	+

- [1] L. Lu, J. D. Joannopoulos, and M. Soljačić, Topological photonics, *Nat. Photonics* **8**, 821 (2014).
- [2] T. Ozawa, H. M. Price, A. Amo, N. Goldman, M. Hafezi, L. Lu, M. C. Rechtsman, D. Schuster, J. Simon, O. Zilberberg, and I. Carusotto, Topological photonics, *Rev. Mod. Phys.* **91**, 015006 (2019).
- [3] A. B. Khanikaev, S. H. Mousavi, W.-K. Tse, M. Kargarian, A. H. MacDonald, and G. Shvets, Photonic topological insulators, *Nat. Mater.* **12**, 233 (2013).
- [4] G. Ma, M. Xiao, and C. T. Chan, Topological phases in acoustic and mechanical systems, *Nat. Rev. Phys.* **1**, 281 (2019).
- [5] X. Ni, M. Li, M. Weiner, A. Alù, and A. B. Khanikaev, Demonstration of a quantized acoustic octupole topological insulator, *Nat. Commun.* **11**, 2108 (2020).
- [6] C. He, H.-S. Lai, B. He, S.-Y. Yu, X. Xu, M.-H. Lu, and Y.-F. Chen, Acoustic analogues of three-dimensional topological insulators, *Nat. Commun.* **11**, 2318 (2020).

- [7] M. Oudich, N. J. Gerard, Y. Deng, and Y. Jing, Tailoring structure-borne sound through bandgap engineering in phononic crystals and metamaterials: A comprehensive review, *Adv. Funct. Mater.* **33**, 2206309 (2023).
- [8] L. Xin, Y. Siyuan, L. Harry, L. Minghui, and C. Yan feng, Topological mechanical metamaterials: A brief review, *Curr. Opin. Solid State Mater. Sci.* **24**, 100853 (2020).
- [9] H. Huang, J. Chen, and S. Huo, Recent advances in topological elastic metamaterials, *J. Phys.: Condens. Matter* **33**, 503002 (2021).
- [10] M. Miniaci, R. K. Pal, R. Manna, and M. Ruzzene, Valley-based splitting of topologically protected helical waves in elastic plates, *Phys. Rev. B* **100**, 024304 (2019).
- [11] M. Proctor, P. A. Huidobro, B. Bradlyn, M. B. de Paz, M. G. Vergniory, D. Bercioux, and A. García-Etxarri, On the robustness of topological corner modes in photonic crystals, *Phys. Rev. Res.* **2**, 042038 (2020).
- [12] Y. Jin, D. Torrent, and B. Djafari-Rouhani, Robustness of conventional and topologically protected edge states in phononic crystal plates, *Phys. Rev. B* **98**, 054307 (2018).
- [13] Z. H. Wen, S. X. Zeng, D. W. Wang, Y. B. Jin, and R. B. Djafari, Robust edge states of subwavelength chiral phononic plates, *Extreme Mech. Lett.* **44**, 101209 (2021).
- [14] Y. Chen, X.-T. He, Y.-J. Cheng, H.-Y. Qiu, L.-T. Feng, M. Zhang, D.-X. Dai, G.-C. Guo, J.-W. Dong, and X.-F. Ren, Topologically Protected Valley-Dependent Quantum Photonic Circuits, *Phys. Rev. Lett.* **126**, 230503 (2021).
- [15] S. Y. Yu, C. He, Z. Wang, F. K. Liu, X. C. Sun, Z. Li, H. Z. Lu, M. H. Lu, and Y. F. Chen, Elastic pseudospin transport for integratable topological phononic circuits, *Nat. Commun.* **9**, 3072 (2018).
- [16] H. Chen, L. Y. Yao, H. Nassar, and G. L. Huang, Mechanical Quantum Hall Effect in Time-Modulated Elastic Materials, *Phys. Rev. Appl.* **11**, 044029 (2019).
- [17] M. Miniaci, P. K. Pal, B. Morvan, and M. Ruzzene, Experimental Observation of Topologically Protected Helical Edge Modes in Patterned Elastic Plates, *Phys. Rev. X* **8**, 031074 (2018).
- [18] S. H. Mousavi, A. B. Khanikaev, and Z. Wang, Topologically protected elastic waves in phononic metamaterials, *Nat. Commun.* **6**, 8682 (2015).
- [19] Z. D. Zhang, S. Y. Yu, H. Ge, J. Q. Wang, H. F. Wang, K. F. Liu, T. Wu, C. He, M. H. Lu, and Y. F. Chen, Topological Surface Acoustic Waves, *Phys. Rev. Appl.* **16**, 044008 (2021).
- [20] J. Vila, R. K. Pal, and M. Ruzzene, Observation of topological valley modes in an elastic hexagonal lattice, *Phys. Rev. B* **96**, 134307 (2017).
- [21] M. Serra-Garcia, V. Peri, R. Süsstrunk, O. R. Bilal, T. Larsen, L. G. Villanueva, and S. D. Huber, Observation of a phononic quadrupole topological insulator, *Nature* **555**, 342 (2018).
- [22] Z. Liu, X. Zhang, Y. Mao, Y. Y. Zhu, Z. Yang, C. T. Chan, and P. Sheng, Locally resonant sonic materials, *Science* **289**, 1734 (2000).
- [23] Y. Jin, Y. Pennec, B. Bonello, H. Honarvar, L. Dobrzynski, B. Djafari-Rouhani, and M. I. Hussein, Physics of surface vibrational resonances: Pillared phononic crystals, metamaterials, and metasurfaces, *Rep. Prog. Phys.* **84**, 086502 (2021).
- [24] L. Y. Cao, Z. C. Yang, Y. L. Xu, and B. M. Assouar, Deflecting flexural wave with high transmission by using pillared elastic metasurface, *Smart Mater. Struct.* **27**, 075051 (2018).
- [25] L. Cao, Z. Yang, Y. Xu, Z. Chen, Y. Zhu, S.-W. Fan, K. Donda, B. Vincent, and B. Assouar, Pillared elastic metasurface with constructive interference for flexural wave manipulation, *Mech. Syst. Signal Process.* **146**, 107035 (2021).
- [26] R. Chaunsali, C. W. Chen, and J. Yang, Experimental demonstration of topological waveguiding in elastic plates with local resonators, *New J. Phys.* **20**, 113036 (2018).
- [27] R. K. Pal and M. Ruzzene, Edge waves in plates with resonators: An elastic analogue of the quantum valley Hall effect, *New J. Phys.* **19**, 025001 (2017).
- [28] R. Chaunsali, C. W. Chen, and J. Yang, Subwavelength and directional control of flexural waves in zone-folding induced topological plates, *Phys. Rev. B* **97**, 054307 (2018).
- [29] Q. Zhang, Y. Chen, K. Zhang, and G. Hu, Dirac degeneracy and elastic topological valley modes induced by local resonant states, *Phys. Rev. B* **101**, 014101 (2020).
- [30] T. Lee and H. Iizuka, Bragg scattering based acoustic topological transition controlled by local resonance, *Phys. Rev. B* **99**, 064305 (2019).
- [31] Y. Tang, B. Liang, J. Yang, J. Yang, and J.-C. Cheng, Topological phononic crystals with tunable interface state based on local resonance, *Appl. Phys. Express* **12**, 094002 (2019).
- [32] D. Qi, Z. Ren, and Z. Qu, Valley-protected topological interface state of the elastic wave: From discrete model to multistable mechanical metamaterials, *J. Sound Vib.* **529**, 116908 (2022).
- [33] H. Huang, S. Huo, and J. Chen, Subwavelength elastic topological negative refraction in ternary locally resonant phononic crystals, *Int. J. Mech. Sci.* **198**, 106391 (2021).
- [34] W. Fang, C. Han, Y. Chen, and Y. Liu, Valley Hall elastic edge states in locally resonant metamaterials, *Materials* **15**, 1491 (2022).
- [35] L. Fan, Y. He, X. Zhao, and X.-A. Chen, Subwavelength and broadband tunable topological interface state for flexural wave in one-dimensional locally resonant phononic crystal, *J. Appl. Phys.* **127**, 235106 (2020).
- [36] H.-B. Huang, J.-J. Chen, and S.-Y. Huo, Simultaneous topological Bragg and locally resonant edge modes of shear horizontal guided wave in one-dimensional structure, *J. Phys. D: Appl. Phys.* **50**, 275102 (2017).
- [37] S. Y. Huo, J. J. Chen, H. B. Huang, and G. L. Huang, Simultaneous multi-band valley-protected topological edge states of shear vertical wave in two-dimensional phononic crystals with veins, *Sci. Rep.* **7**, 10335 (2017).
- [38] Z. Huang, J. Wu, C. Wang, S. Yang, and F. Ma, Resonant-scattering hybrid device for multiband acoustic topology valley transmission, *Phys. Rev. B* **104**, 094110 (2021).
- [39] Z. Zhang, S. Yu, M. Lu, and Y. Chen, Dual-Band Helical Edge States and Discrete Dirac Vortices in Solid-State Elastic Waves, *Phys. Rev. Appl.* **17**, 034029 (2022).
- [40] X. Huang, Y. Yan, J. Ma, J. Li, and X. Rui, An acoustic metamaterial-based sensor capable of multiband filtering and amplification, *IEEE Sens. J.* **20**, 4413 (2020).

- [41] Y. Chen, Z. Lan, Z. Su, and J. Zhu, Inverse design of photonic and phononic topological insulators: A review, *Nanophotonics* **11**, 4347 (2022).
- [42] Y. Chen, Z. Lan, and J. Zhu, Inversely Designed Second-Order Photonic Topological Insulator with Multiband Corner States, *Phys. Rev. Appl.* **17**, 054003 (2022).
- [43] B.-Y. Xie, H.-F. Wang, H.-X. Wang, X.-Y. Zhu, J.-H. Jiang, M.-H. Lu, and Y.-F. Chen, Second-order photonic topological insulator with corner states, *Phys. Rev. B* **98**, 205147 (2018).
- [44] Y. Chen, Z. Lan, and J. Zhu, Second-order topological phases in C_{4v} -symmetric photonic crystals beyond the two-dimensional Su-Schrieffer-Heeger model, *Nanophotonics* **11**, 1345 (2022).
- [45] X. Zhang, H. X. Wang, Z. K. Lin, Y. Tian, B. Xie, M. H. Lu, Y. F. Chen, and J. H. Jiang, Second-order topology and multidimensional topological transitions in sonic crystals, *Nat. Phys.* **15**, 582 (2019).
- [46] Z. Zhang, H. Long, C. Liu, C. Shao, Y. Cheng, X. Liu, and J. Christensen, Deep-subwavelength holey acoustic second order topological insulators, *Adv. Mater.* **31**, 1904682 (2019).
- [47] C. Chen, T. Chen, W. Ding, X. Xiang, F. Mao, and J. Zhu, Split-ring resonator coupling-induced tunable acoustic second-order topological insulators, *Phys. Rev. B* **106**, 045403 (2022).
- [48] X.-D. Chen, W.-M. Deng, F.-L. Shi, F.-L. Zhao, M. Chen, and J.-W. Dong, Direct Observation of Corner States in Second-Order Topological Photonic Crystal Slabs, *Phys. Rev. Lett.* **122**, 233902 (2019).
- [49] Y. Chen, J. Li, and J. Zhu, Topology optimization of quantum spin Hall effect-based second-order phononic topological insulator, *Mech. Syst. Signal Process.* **164**, 108243 (2022).
- [50] H. Xue, Y. Yang, F. Gao, Y. Chong, and B. Zhang, Acoustic higher-order topological insulator on a kagome lattice, *Nat. Mater.* **18**, 108 (2019).
- [51] H. Fan, B. Xia, Liang Tong, S. Zheng, and D. Yu, Elastic Higher-Order Topological Insulator with Topologically Protected Corner States, *Phys. Rev. Lett.* **122**, 204301 (2018).
- [52] C. W. Chen, R. Chaunsali, J. Christensen, G. Theocharis, and J. Yang, Corner states in a second-order mechanical topological insulator, *Commun. Mater.* **2**, 62 (2021).
- [53] Z. Zheng, J. Yin, J. Wen, and D. Yu, Higher-order topological states in locally resonant elastic metamaterials, *Appl. Phys. Lett.* **120**, 144101 (2022).
- [54] S. An, T. Liu, H. Fan, H. Gao, Z. Gu, S. Liang, S. Huang, Y. Zheng, Y. Chen, L. Cheng, and J. Zhu, Second-order elastic topological insulator with valley-selective corner states, *Int. J. Mech. Sci.* **15**, 107337 (2022).
- [55] Q. Wu, H. Chen, X. Li, and G. Huang, In-Plane Second-Order Topologically Protected States in Elastic Kagome Lattices, *Phys. Rev. Appl.* **14**, 014084 (2020).
- [56] Z. Wang, Q. Wei, H. Y. Xu, and D. J. Wu, A higher-order topological insulator with wide bandgaps in Lamb-wave systems, *J. Appl. Phys.* **127**, 075105 (2020).
- [57] Y. Wu, M. Yan, Z. K. Lin, H. X. Wang, F. Li, and J. H. Jiang, On-chip higher-order topological micromechanical metamaterials, *Sci. Bull.* **66**, 1959 (2021).
- [58] S. Huo, H. Huang, L. Feng, and J. Chen, Edge states and corner modes in second-order topological phononic crystal plates, *Appl. Phys. Express* **12**, 094003 (2019).
- [59] X.-P. Song, T.-N. Chen, C. Chen, and W. Ding, Observation of frequency band-switchable topological edge modes using a 2 bit coding acoustic topological insulator, *J. Phys. D: Appl. Phys.* **54**, 255302 (2021).
- [60] X. S. Su and A. N. Norris, Focusing, refraction, and asymmetric transmission of elastic waves in solid metamaterials with aligned parallel gaps, *J. Acoust. Soc. Am.* **139**, 3386 (2016).
- [61] H. X. Wang, G. Y. Guo, and J. H. Jiang, Band topology in classical waves: Wilson-loop approach to topological numbers and fragile topology, *New. J. Phys.* **21**, 093029 (2019).
- [62] G. J. Chaplain, J. M. De Ponti, G. Aguzzi, A. Colombi, and R. V. Craster, Topological Rainbow Trapping for Elastic Energy Harvesting in Graded Su-Schrieffer-Heeger Systems, *Phys. Rev. Appl.* **14**, 054035 (2020).
- [63] R. J. Watkins, S. Santillan, J. Radice, and O. Barton Jr, Vibration response of an elastically point-supported plate with attached masses, *Thin Wall Struct.* **48**, 519 (2010).
- [64] A. Ragonese and M. Nouh, Prediction of local resonance band gaps in 2D elastic metamaterials via Bloch mode identification, *Wave Motion* **105**, 102734 (2021).
- [65] Y. Chen, F. Meng, and X. Huang, Creating acoustic topological insulators through topology optimization, *Mech. Syst. Signal Process.* **146**, 107054 (2021).